The Astrophysical Journal, 615:259–274, 2004 November 1

HIGH-ENERGY DEUTERON MEASUREMENT WITH THE CAPRICE98 EXPERIMENT

P. Papini, S. Piccardi, P. Spillantini, and E. Vannuccini[1]
Dipartimento di Fisica dell'Università and Sezione INFN di Firenze, Via G. Sansone 1, I-50100 Sesto Fiorentino, Florence, Italy

M. Ambriola, R. Bellotti, F. Cafagna, F. Ciacio, M. Circella, and C. N. De Marzo
Dipartimento di Fisica dell'Università and Sezione INFN di Bari, Via Amendola 173, I-70126 Bari, Italy

S. Bartalucci and M. Ricci
Laboratori Nazionali INFN, Via Enrico Fermi 40, CP 13, I-00044 Frascati, Italy

D. Bergström, P. Carlson, T. Francke, P. Hansen, and E. Mocchiutti
Royal Institute of Technology (KTH), 10691 Alba Nova University Center, Stockholm, Sweden

M. Boezio, V. Bonvicini, P. Schiavon, A. Vacchi, and N. Zampa
Dipartimento di Fisica dell'Università and Sezione INFN di Trieste, Via A. Valerio 2, I-34147 Trieste, Italy

U. Bravar and S. J. Stochaj
New Mexico State University, Box 3-PAL, Las Cruces, NM 88003

M. Casolino, M. P. De Pascale, A. Morselli, P. Picozza, and R. Sparvoli
Dipartimento di Fisica dell'Università and Sezione INFN di Roma, Tor Vergata, Via della Ricerca Scientifica 1, I-00133 Rome, Italy

M. Hof, J. Kremer, W. Menn, and M. Simon
Universität Siegen, Walter-Flex-Strasse 3, D-57068 Siegen, Germany

J. W. Mitchell, J. F. Ormes, S. A. Stephens, and R. E. Streitmatter
NASA Goddard Space Flight Center, Code 661, Greenbelt, MD 20771

and

M. Suffert
Centre des Recherches Nuclèaires, BP20, F-67037 Strasbourg Cedex, France
Received 2004 January 29; accepted 2004 June 23

ABSTRACT

We report the first measurement of the deuterium abundance in cosmic rays above 10 GeV nucleon^{-1} of kinetic energy. The data were collected by the balloon-borne experiment CAPRICE98, which was flown on 1998 May 28–29 from Fort Sumner, New Mexico. The detector configuration included the NMSU-WiZard/CAPRICE superconducting magnet spectrometer equipped with a gas RICH detector, a silicon-tungsten calorimeter, and a time-of-flight system. By combining the information from the spectrometer and the RICH detector, it was possible to separate deuterons from protons in the kinetic energy range from 12 to 22 GeV nucleon^{-1}. In order to estimate the proton background and the deuteron selection efficiency, we developed an empirical model for the response of the instrument, based on the data collected in this experiment. The analysis procedure is described in this paper, and the result on the absolute flux of deuterium is presented. We found that the deuterium abundance at high energy is consistent with the hypothesis that the propagation mechanism of light nuclei is the same as that of heavier secondary components.

Subject headings: balloons — cosmic rays — Galaxy: abundances — ISM: abundances

1. INTRODUCTION

The CAPRICE98 (Cosmic Antiparticle Ring-Imaging Cerenkov Experiment, 1998) balloon-borne experiment was launched on 1998 May 28 from Fort Sumner, New Mexico (34°.3 north, 110°.1 west) and landed on May 29 close to Holbroke, Arizona (34°.0 north, 104°.1 west). The average geomagnetic cutoff rigidity for the geographical location of the flight was about 4.3 GV (Shea et al. 1983). The instrument was designed primarily for the cosmic-ray antiprotons. However, the configuration allowed several additional science objectives to be achieved, among which is the measurement of the deuterium abundance.

The main information concerning the propagation mechanism of cosmic rays in the Galaxy is provided by the relative abundances of secondary components and the parent primaries. Since deuterium is significantly rare in astrophysical environments, cosmic-ray deuterium is generally believed to be of secondary origin, produced during the nuclear interactions of cosmic rays with the interstellar medium. As pointed out by Stephens (1989), among several secondary components the specific feature of light secondaries such as ^{2}H and ^{3}He is that their interaction mean free path is considerably larger than the escape mean free path for cosmic rays from the Galaxy. This is not the case for the heavier secondaries, where the escape mean free path is of the same order or greater than their interaction length. As a consequence, light secondaries provide information concerning cosmic-ray interstellar propagation that is complementary to that obtained from the study of heavy secondaries.

In spite of the scientific relevance of these measurements, few experimental results exist, with most of them obtained

[1] Corresponding author; vannucci@fi.infn.it.

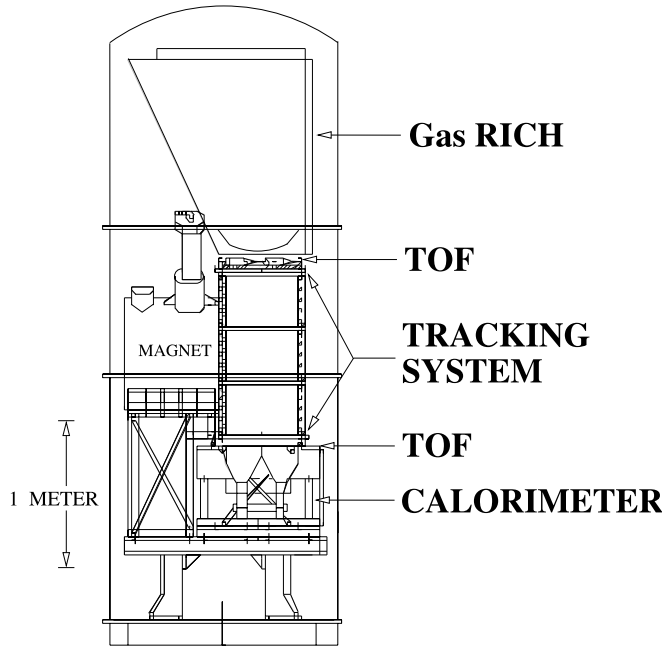

FIG. 1.—Schematic view of the CAPRICE98 apparatus.

below a few GeV nucleon^{-1} of kinetic energy. In this energy domain data are affected by solar modulation and, in the case of balloon-borne experiments, by a large atmospheric background. For these reasons it is more difficult to disentangle from data the interstellar propagation information.

The identification of deuterons with the CAPRICE98 instrument was based on the information given by a gas Ring-Imaging Cherenkov (RICH) detector used as a threshold device. The high velocity threshold for Cerenkov light emission provided by the gas radiator allowed us to measure the deuterium abundance in an energy domain scarcely explored until now. Preliminary results were reported earlier (Vannuccini et al. 2002, 2003b). Here we present the final results on the deuterium flux between 12 and 22 GeV nucleon^{-1}. The instrument configuration is described in § 2, the data analysis is provided in § 3, and the results are reported in § 4. Finally, in the Appendix the methods used to estimate the spectrometer resolution function are described and discussed.

2. THE CAPRICE98 APPARATUS

The CAPRICE98 apparatus was designed to identify particles in the energy range from a few hundred MeV up to hundreds of GeV (Ambriola et al. 1999). The instrument (a schematic view is shown in Fig. 1) was composed of a superconducting magnet spectrometer, complemented by three additional detectors: a RICH detector, a time-of-flight (ToF) system, and an electromagnetic imaging calorimeter. The information provided by these detectors, when combined with that of the spectrometer, enabled particle identification. The RICH detector played a crucial role in the identification of deuterons, and its performance is explained in detail.

2.1. *The Gas RICH Detector*

The RICH detector (Bergström et al. 2001) consisted of a photosensitive multiwire proportional chamber (MWPC), a 1 m tall radiator box filled with high-purity C_4F_{10} gas, and a spherical mirror. When a particle entered the RICH detector, it first traversed the plane that housed the MWPC, then passed through the radiator, where, if its velocity was above the Cerenkov threshold, it eventually produced a cone of light of velocity-dependent width θ_c. The velocity threshold for emission of light is set by the refractive index of the radiator, which was on average $n = 1.0014$ during the flight. This resulted in a threshold rigidity for particles of mass m equal to $R_{\rm th} = (mc/Ze)(\beta\gamma)_{\rm th}$, where $(\beta\gamma)_{\rm th}$ was about 19. The cone of light after traversing the radiator was reflected back and focused by the spherical mirror toward the MWPC, which was separated from the radiator volume by a quartz window. The MWPC was operated with pure ethane saturated with tetrakis-dimethyl-amino-ethylene (TAME) that acted as a photon converter. The upper cathode plane of the MWPC was divided into 64×64 pads of size 8×8 mm^2. Relativistic particles produce a ring-like image approximately 11 cm wide.

The Cerenkov angle (θ_c) was reconstructed offline (Bergström 2000; Bergström et al. 2001) by combining the information of the hit pads, excluding the possible ionization area, with the information on the particle track inside the radiator extrapolated from the tracking system. The value of θ_c was evaluated using the Gaussian potential method (Agakichiev et al. 1996), which uses a weighted average performed over a restricted set of hit pads identified as belonging to the possible ring. This provided particle identification capability based on θ_c versus R selection, where R indicates the measured rigidity. The RICH detector also could be used as a threshold device, by requiring no hit pads. It is worth noting that when the RICH detector was used as a threshold device, the selection was based not only on a "light/no light" condition but also on the information about the expected position of the Cerenkov ring. This enhanced the detector immunity to noise, which was anyway found to be less than one pad hit out of 4096 channels per event (Bergström et al. 2001). A graphical view of different particle signatures in the RICH detector is shown in Figure 2, where the hit patterns of both emitting and nonemitting particles are shown. In the first case the effective number of pads used to evaluate the Cerenkov angle (Bergström 2000; Bergström et al. 2001) was $N_{\rm eff} = 44.9$. In the second case no hit pads due to Cerenkov signal were identified, and as a consequence $N_{\rm eff}$ was set to zero. These features allowed deuterons to be efficiently identified when no Cerenkov signal should appear in the predicted area. Quantitative details concerning the RICH performances are discussed further in §§ 3.2 and 3.3.2.

2.2. *The Magnetic Spectrometer*

The primary task of the spectrometer was to measure the sign and the absolute value of the deflection of particles traversing the apparatus. The CAPRICE98 magnetic spectrometer was composed of a drift chamber tracking system placed in the high-field region of a superconducting magnet.

The magnet (Golden et al. 1978) consisted of a single coil of 11,161 turns of copper-clad Nb-Ti wire of 36 cm inner diameter, 61 cm outer diameter, and 7.6 cm axial thickness. The coil was placed in a Dewar filled with liquid helium, thermally insulated from the rest of the payload. The operating current was 120 A, producing an inhomogeneous field of approximately 4 T at the center of the coil and varying from 1.8 to 0.1 T inside the tracking volume.

The tracking system consisted of three drift chambers, whose design was optimized to work in the presence of a strong magnetic field (Hof et al. 1994). Each chamber had a total inner volume of $47 \times 47 \times 35$ cm^3 and contained five double layers of sense wires, arranged to give six position

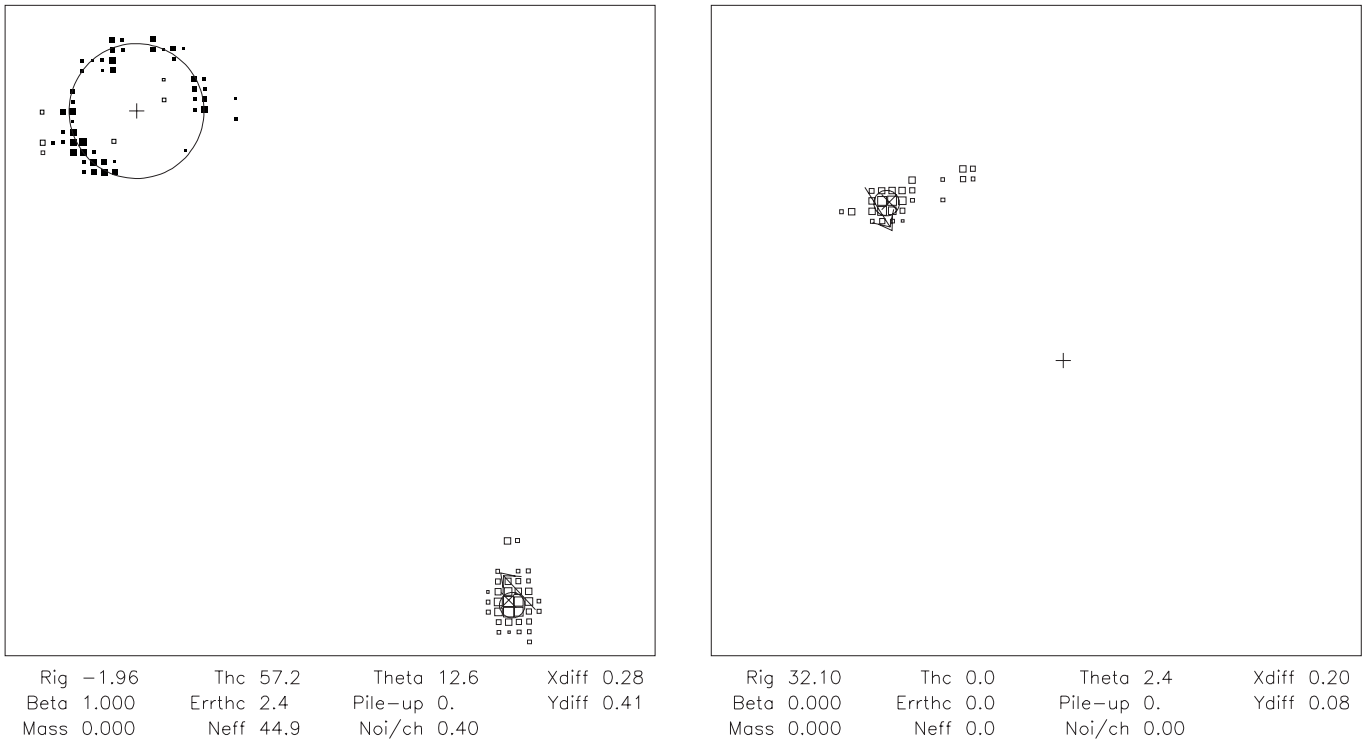

FIG. 2.—Examples of different hit patterns in the RICH pad plane. *Left*: Relativistic electron. Both the ionization cluster and the Cerenkov ring are visible. *Right*: $Z = 1$ particle of measured rigidity 32 GV. The cross indicates the expected position of the Cerenkov ring center. In this case the Cerenkov signal is clearly missing, so the particle is probably a deuteron.

measurements in the bending view and four in the nonbending one. The chambers were operating with pure CO_2 gas, flushed during the flight in order to maintain constant pressure inside the boxes. A high efficiency (about 99% for a single drift cell) and a spatial resolution better than 100 μm were achieved.

The spectrometer configuration allowed a maximum detectable rigidity (MDR, defined as the rigidity value for which the relative error on the measured rigidity is equal to 1), for the selection cuts applied in this analysis, of about 400 GV. More details concerning the spectrometer resolution are discussed further in § 3.3.1 and the Appendix.

2.3. *The Time-of-Flight System*

The ToF system consisted of two layers of plastic scintillators, 1.19 m apart, placed above and below the tracking system, respectively. Each plane was composed of two 25×50 cm^2 paddles, each one viewed edge-on by two phototubes. The ToF time resolution was 230 ps.

The ToF provided both time and energy-loss information. The scintillator signals also provided the trigger for the data acquisition.

2.4. *The Calorimeter*

The calorimeter was designed (Bocciolini et al. 1996; Ricci et al. 1999) to provide high identification capability of electromagnetic showers in a large background of noninteracting particles and interacting hadrons. It consisted of eight silicon-sensor planes interleaved with seven layers of tungsten absorber. Each sensor layer was a matrix of 8×8 silicon modules having an active area of 6×6 cm^2. A single module was composed by two silicon sensors, 380 μm thick, divided into 16 strips. The sensors were mounted back to back with perpendicular strips in order to provide double-coordinate readout. The total depth was 7.2 radiation lengths and 0.33 hadronic interaction lengths.

The high segmentation of the calorimeter, in both longitudinal and transverse directions, combined with the energy-loss information provided by the silicon detectors, offered several criteria for particle identification (Boezio 1998).

3. DATA ANALYSIS

The analysis was based on 21 hr of data for a total acquisition time of 67,240 s under an average residual atmosphere of 5.5 g cm^{-2}. The fractional live time during the flight was $48.65\% \pm 0.02\%$, resulting in a total live time $T_{\rm live} = 32{,}712 \pm 13$ s.

Hydrogen is the most abundant element in the cosmic radiation. Deuterium represents only a small fraction of the hydrogen flux, with protons being the dominant isotopic component. Besides galactic cosmic rays, balloon data also contain secondary particles produced in particle interactions in both the residual atmosphere and the instrument material. These interactions lead to the production of mainly singly charged particles such as protons, pions, muons, a small fraction of electrons and positrons, and deuterons.

3.1. *Proton and Deuteron Selection*

The data set used for the deuterium analysis consisted of positive singly charged particles with a well-reconstructed track in the spectrometer and a trajectory contained inside the sensitive volume of the detectors. Since the calorimeter had no role in the deuterium identification, no constraints were imposed on its response. The applied basic selection criteria are listed in Table 1.

TABLE 1

SUMMARY OF SELECTION CRITERIA FOR POSITIVE SINGLY CHARGED PARTICLES

Cut	Description
Tracking system selection:	
1	At least 11 position measurements in the (maximum bending) x-direction and 7 in the y-direction used in the fit
2	Conditions on the χ^2 for the fitted track: $\chi^2_x < 4$ and $\chi^2_y < 8$
3	Deflection uncertainty less than 0.008 GV^{-1}
4	Positive deflection
5[a]	Containment of the track inside the tracking volume
Scintillators and ToF selection:	
6	Downward-moving particles
7	dE/dx losses in the top scintillator less than 1.8 mip
8	Only one paddle hit in the top scintillator
RICH detector selection:	
9	If the particle crossed the MWPC, only one ionization cluster in the location indicated by the tracking system
10	If the particle crossed the MWPC, difference between the extrapolated track and the center of gravity of the ionization cluster less than 3 σ
11[a]	Extrapolated track not intersecting the support frame of the MWPC
12[a]	Center of the expected Cerenkov ring contained in the pad plane, excluding an outer frame of $\sim$5 cm

[a] These geometrical conditions are accounted for in the geometrical factor.

Deuterons were selected from the resulting event sample by requiring no Cerenkov signal in the RICH above the proton threshold rigidity.

3.1.1. *Tracking*

A reliable measurement of the particle rigidity was very important for the deuterium analysis, since the finite resolution of the spectrometer significantly affects the proton background distribution. As an example, owing to the uncertainty in the measured deflection, a rigidity value greater than the threshold for Cerenkov light emission could be assigned to a proton with rigidity under the threshold, therefore satisfying the condition for the deuterium selection. For this reason strict selection criteria were imposed on the quality of the fitted tracks.

The tracking selection criteria have been extensively studied in previous works related to the same experiment (Boezio et al. 2001, 2003a) and to other similar tracking systems (Hof et al. 1996; Mitchell et al. 1996; Boezio et al. 1997). The selection cuts used in this analysis, partly based on the gained experience, were chosen as a compromise between a good track reconstruction and enough statistics for the analysis.

A minimum number of position measurements were required on both the bending and nonbending views. The quality of the fitted track is characterized by the resulting χ^2. As a consequence, an acceptable χ^2 was required in both directions with a stronger constraint on the x-direction (see Table 1). In addition to the above criteria, a further condition on the deflection uncertainty, calculated on an event-by-event basis by the fitting routine (Golden et al. 1991), was imposed.

3.1.2. *Scintillators and Time of Flight*

The information of the ToF system was used to select downward-moving particles. The dE/dx information from the top scintillator was used to select singly charged particles, as well as to reject the multiparticle events coming from interactions above the top scintillator. The bottom scintillator was not used in the charge selection since it could collect signals from backscattered particles from the calorimeter. These events were found not to affect the performances of the spectrometer; therefore, in order to maximize the statistic, no conditions were imposed on the signal from the bottom scintillator.

3.1.3. *RICH Detector*

The tracking capabilities of the RICH MWPC were used to eliminate multiparticle events. An ionizing particle induces in the MWPC a signal that is typically 10 times larger (Bergström et al. 2001) than the signal induced by a Cerenkov photon. This provided a criterion to identify and reject multiparticle events, by requiring no ionization clusters outside the area surrounding the track, extrapolated from the tracking system up to the pad-plane level. For those tracks traversing the MWPC (about 46% of the events), the center of gravity of the ionization cluster was required to be consistent with the position of the track intersection point (Boezio et al. 2003a).

The deuterium selection criterion was based on the fact that deuterons start to emit Cerenkov light above 35 GV of rigidity, while lighter singly charged particles have a lower Cerenkov threshold. In the rigidity range between the proton threshold, 18 GV, and the deuterium threshold the RICH detector could be used to identify deuterons. In order to ensure that if Cerenkov light was emitted it could be fully detected, the center of the Cerenkov ring, calculated using the tracking information, was required to be contained inside an inner perimeter in the pad plane. The size of the excluded frame was about 5 cm, which corresponds to about the radius of the maximum Cerenkov ring.

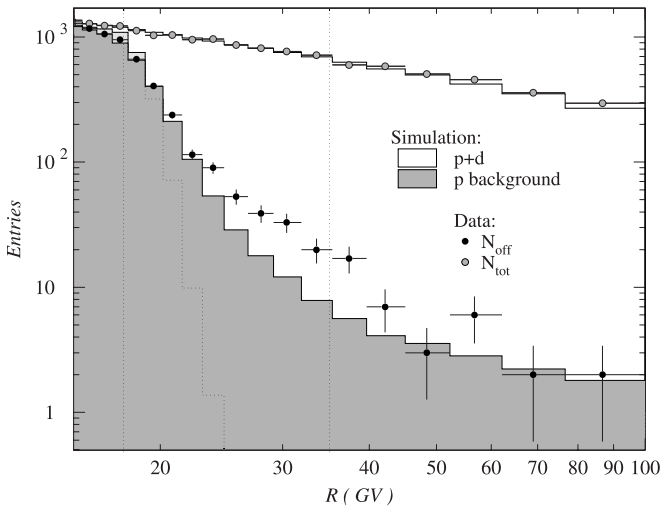

FIG. 3.—Distribution of the selected events (*circles*) as a function of the measured rigidity compared with the simulated background distribution (*dark gray histogram*). The light gray histogram shows the simulated distribution of protons without Cerenkov signal obtained without including the spectrometer uncertainty. The vertical dotted lines indicate the proton and deuteron threshold rigidities.

The RICH detector information was used to select deuterons out of the surviving positive singly charged particle sample by requiring $N_{\rm eff} = 0$. This condition allows, in principle, deuterons to be distinguished from lighter particles above the proton threshold rigidity. Figure 3 shows the rigidity distribution of the selected positive singly charged particle events ($N_{\rm tot}$) and of those events without a Cerenkov signal ($N_{\rm off}$). The number of events without a Cerenkov signal drops above the proton threshold (18 GV). For increasing rigidities, the distribution flattens while approaching the deuteron Cerenkov threshold (35 GV) and drops again above it. The rigidity region when the distribution flattens indicates the range where the deuteron component outnumbers the proton background. The proton contamination is significant over the whole rigidity range; thus, in order to determine the deuteron component, this contamination must be estimated and subtracted. Since the RICH is the only detector that gives information that can be used to identify the deuterium, the deuteron selection criterion could not be cross-checked using the other devices. Therefore, the background level and the deuteron selection efficiency were estimated by means of simulation.

3.2. *RICH Performances*

The RICH detector had a key role in the deuterium analysis. For this reason its response was carefully studied. We report in this section some general results that were used to tune the simulation, described further in § 3.3.

According to the Cerenkov theory, the mean number of detected Cerenkov photoelectrons and the angle θ_c are, for singly charged particles, independent of the particle type if expressed as a function of β, or equivalently $R/R_{\rm th}$. The main features of the Cerenkov effect can be expressed through the following relation:

$$\frac{N_{\rm pe}}{N_{\rm pe}^{\max}} = \frac{\sin^2\theta_c}{\sin^2\theta_c^{\max}} = 1 - \left(\frac{R_{\rm th}}{R}\right)^2, \qquad (1)$$

which states that both the quantities $\sin^2\theta_c$ and $N_{\rm pe}$ increase for increasing rigidity starting from zero at the threshold up to an asymptotic value. The maximum value $\theta_c^{\rm max}$ of the Cerenkov angle depends only on the refractive index n of the medium, while $N_{\rm pe}^{\rm max}$ depends also on the response parameter N_0 of the instrument. This is characteristic of the photon detector and is related to the mean number of detected photoelectrons by the relation $N_{\rm pe} = N_0 L Z^2 \sin^2\theta_c$, where L is the length of the radiator and Z is the charge of the incoming particle.

The RICH performances were studied using a large sample of muons from data collected at ground prior to the flight. Muons were selected by applying all the basic cuts, listed in Table 1, plus the requirement of a noninteracting path in the calorimeter. This allowed the RICH response to be studied without the complications arising from the presence of significant components of particles of different types. A further advantage of using muons was that their Cerenkov rigidity threshold is about 10 times smaller than that of protons; as a consequence, the spectrometer effect for muons was strongly reduced. Thanks to the scaling property of the Cerenkov effect, all the quantities related to the RICH response could be parameterized as a function of $R/R_{\rm th}$ for muons and then scaled to particles of different type by calculating the proper Cerenkov rigidity thresholds $R_{\rm th}$.

The overall performance of the RICH detector is strictly connected to the mean number of detected photoelectrons. The greater this number is, the lower the error on the measured angle. A large number of detected photoelectrons is also important if the RICH detector is used as a threshold device, since the identification capability is affected by Poisson fluctuations. The quantity $N_{\rm pe}^{\rm max}$ was evaluated from the mean effective number of pads $N_{\rm eff}$ used in the Cerenkov angle reconstruction for a sample of relativistic negative muons as described by Bergström et al. (2001). The resulting value, for the selection cuts applied in this analysis, was $N_{\rm pe}^{\rm max} = 20.6 \pm 1.7$, corresponding to a response parameter $N_0 = 82$ cm^{-1}. The distribution of the reconstructed Cerenkov angles was, to a good approximation, Gaussian. This distribution had a rigidity-dependent sigma, which was 1.07 mrad for events where the maximum number of photoelectrons was produced (Vannuccini 2001).

The RICH performances inferred from ground muons could not be used to simulate the in-flight behavior of the detector, as a result of different pressure and temperature of the gas radiator during the flight. Both the refractive index and the photoelectron absorption length of the radiator were different than at ground. The variation of the gas radiator conditions resulted in a slightly higher value of $\theta_c^{\rm max}$, as a result of the increase of the refractive index. The parameter $N_{\rm pe}^{\rm max}$, which is also related to the photon transmission factor of the radiator, was instead lower. The estimated value from relativistic flight particles was $N_{\rm pe}^{\rm max} = 16.6 \pm 2.3$, corresponding to a response parameter $N_0 = 60$ cm^{-1}. The RICH response in flight is compared with that at ground in Figure 4, where the mean effective number $N_{\rm eff}$ of pads used in the Cerenkov angle fit is plotted as a function of squared sine of the measured angle for ground muons and flight protons.

In the following it is implicitly assumed that all the RICH-related quantities parameterized using ground muons were properly scaled to flight on the basis of the measured maximum number of detected photoelectrons.

3.3. *Instrument Simulation*

The presence of protons without a Cerenkov signal with measured rigidity above the threshold for Cerenkov light emission is an effect related to both the RICH detector and the spectrometer responses. The number of detected photoelectrons is affected by statistical fluctuations around a mean value $N_{\rm pe}$ that is zero at the threshold and increases with rigidity up to an asymptotic value. It follows that, even if the proton rigidity was above the threshold, the number of detected photoelectrons could be equal to zero. The probability to detect zero photoelectrons is rigidity dependent and decreases for increasing $N_{\rm pe}$. Moreover, also the finite resolution of the spectrometer, whose effect is the broadening of the rigidity distribution of protons without a Cerenkov signal, contributed to the presence of background protons. Both the above effects led to a substantial contamination of protons in the deuteron sample, as can be seen in Figure 3.

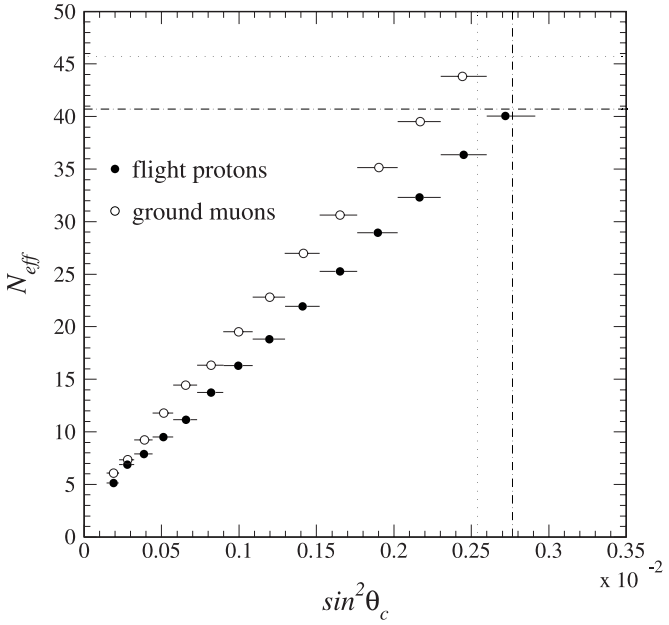

FIG. 4.—Mean effective number of pads used in the Cerenkov angle reconstruction as a function of the squared sine of the measured angle, obtained from ground muons (*open circles*) and flight protons (*filled circles*). Dotted and dot-dashed lines indicate the asymptotic values of $N_{\rm eff}$ and $\sin^2\theta_c$ estimated as described in the text.

In order to obtain the proton background distribution, a Monte Carlo approach was used. The RICH detector response was simulated by using the probability of having no Cerenkov signal ($P_{\rm off}$), and the spectrometer response was simulated by using its resolution function (SRF). Both of these quantities were first derived from experimental data and hence used as input to the simulation.

3.3.1. *Spectrometer Resolution Function*

Two methods were developed and applied to parameterize the high-energy spectrometer response: the magnet-off and the RICH methods. In the following both methods are briefly described (a more detailed discussion can be found in the Appendix):

1. *Magnet-off method*.—This method is based on the measurement of straight tracks collected with the magnet off; if these events are analyzed as if they were high-rigidity particles, the resulting deflection distribution gives directly the SRF. When dealing with magnet-off data, high-energy particles could be selected by requiring a high value of the measured Cerenkov angle in the RICH detector. The selected particle sample contained mainly muons with rigidity greater than $\sim$5 GV, which

still suffered from a residual multiple-scattering effect. An improved estimate of the high-energy SRF was obtained by unfolding the contribution due to the multiple-scattering effect from the experimental deflection distribution.

2. *RICH method*.—A different approach to the problem of evaluating the SRF at high energy used protons above the threshold for Cerenkov light emission from flight data. For particles having a Cerenkov signal in the RICH, an independent estimate of the deflection is available from the measured Cerenkov angle, if the mass is known. The SRF was derived from the distribution of the difference between the deflection calculated from the measured Cerenkov angle and the deflection measured by the spectrometer. This distribution represents the SRF folded with the deflection resolution function of the RICH detector, which was constructed as described in the Appendix.

Both methods provided reliable estimates of the SRF, which are, however, significantly different. Since there are no strong indications in favor of one of the two methods (see the discussion in the Appendix), we carried on the simulation using both of the evaluated functions; the simulation outputs were averaged and the difference with the average was taken as an estimate of the systematic uncertainty. This argument is discussed in more detail in § 3.8.

3.3.2. *Probability of Zero Detected Photoelectrons*

Since the probability $P_{\rm off}$ of having no Cerenkov signal in the RICH detector depends only on the mean number of detected Cerenkov photoelectrons, it was parameterized using ground muons as a function of $R/R_{\rm th}$ and scaled to flight protons and deuterons. Only negative muons were used; positive muons were excluded because of the residual contamination of protons.

An estimate of $P_{\rm off}$ could be obtained, neglecting the deflection uncertainty, from the fraction of muons without a Cerenkov signal ($N_{\rm eff} = 0$). Nevertheless, the spectrometer also gave for muons a small but finite effect. Since this would affect the estimate of the proton background distribution, $P_{\rm off}$ was derived from the distribution of muons without a Cerenkov signal after unfolding of the spectrometer response. The unfolding procedure required knowledge of the low-energy SRF, which was constructed on an event-by-event basis running the GEANT code described in the Appendix. In order to visualize the effect of the spectrometer on the muon distribution, the observed fraction of muons without a Cerenkov signal (*filled circles*) is compared in Figure 5 with the estimated expression for $P_{\rm off}$ (*solid curve*). The expression used to parameterize $P_{\rm off}$ is

$$P_{\rm off}(R/R_{\rm th}) = P_0 e^{-\tilde{N}_{\rm pe}(R/R_{\rm th})}, \qquad (2)$$

where $\tilde{N}_{\rm pe}$ is the mean number of detected photoelectrons and is given by

$$\tilde{N}_{\rm pe}\left(\frac{R}{R_{\rm th}}\right) = N_{\rm pe}^{\rm max}\left[1 - \left(\frac{R_{\rm th}}{R}\right)^2\right] \times \left[1 + \exp\left(\frac{c_1 - R/R_{\rm th}}{c_2}\right)\right]^{-1}. \qquad (3)$$

Equation (2) is the product between the Poisson probability of zero detected Cerenkov photoelectrons, where the expected number is $\tilde{N}_{\rm pe}$, and the probability P_0 of having no signal induced by other causes, e.g., MWPC noise. In equation (3), $N_{\rm pe}^{\rm max}$ is the maximum number of detected Cerenkov photoelectrons and the second term expresses the dependence on rigidity of the mean number of emitted photons, according to equation (1). Both P_0 and $N_{\rm pe}^{\rm max}$ were independently evaluated. The procedure used to estimate the maximum number of detected photoelectrons and the resulting value is described in § 2.1. The probability of having no signal in the MWPC induced by other causes than Cerenkov photoelectrons was estimated using ground muons under the threshold for Cerenkov light emission. The obtained value was $P_0 = 0.962 \pm 0.006$.

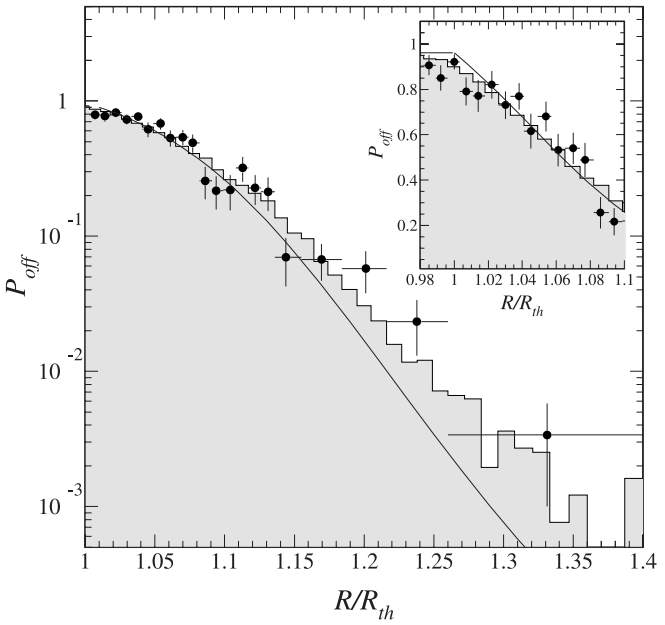

FIG. 5.—Fraction of muons without a Cerenkov signal as a function of $R/R_{\rm th}$. *Filled circles*: Negative muons from ground data. *Gray histogram*: Simulated sample of muons; the RICH detector response was generated according to $P_{\rm off}$ and the rigidity smeared according to the low-energy SRF. *Solid curve*: Estimated expression for $P_{\rm off}$.

The last term in equation (3) is an empirical factor introduced to reproduce the experimental data; the RICH detector behaved as if the photon detection efficiency increased for increasing particle rigidity, starting from the threshold up to an asymptotic value, which resulted in $N_{\rm pe}^{\rm max}$ detected photoelectrons. The only process, starting from the emission of Cerenkov light to the production of a detectable signal, that can account for this behavior is the photoelectron detection in the MWPC. In particular, a nonuniform response of the detector could explain what we observed. In fact, only when the diameter of the ring is greater that the spatial dimensions over which the detector response varies can an effective efficiency be defined. In this case, the RICH response can be described in terms of the number of detected photoelectrons $N_{\rm pe}^{\rm max}$ estimated for relativistic particles. If instead the ring diameter is of the same order of magnitude of the nonhomogeneities or lower, which happens close to the emission threshold, it can be shown (Vannuccini 2001) that this results in a higher probability of detecting zero photoelectrons. A nonhomogeneous response of the pad plane was actually observed by studying the amplitude of the signals induced by ionizing particles. As a consequence, our approach was to take as the best estimate of $P_{\rm off}$ equations (2) and (3), with parameters c_1 and c_2 set, respectively, to 1.149 and 0.088, values obtained by fitting experimental data. The unfolding procedure was

TABLE 2
SUMMARY OF DEUTERIUM SELECTION RESULTS

RIGIDITY (GV)	NUMBER OF SELECTED EVENTS		ESTIMATED NUMBER OF BACKGROUND PROTONS, $N_{p,\mathrm{off}} = \epsilon_p N_p$	ESTIMATED NUMBER OF DEUTERONS, N_d
	N_{tot}	N_{off}		
27.6–31.9	1578	72	30.1 ± 0.7	46.4 ± 9.2
31.9–45.1	1894	44	17.8 ± 0.6	46.6 ± 11.5

applied using both estimates of the SRF described in § 3.3.1. The variation in the expression of P_{off} was consistent with the errors of the fit.

The value of P_0 and the response of the MWPC were found to be the same in flight and at ground. As a consequence, P_{off} was scaled to flight conditions only by scaling $N_{\mathrm{pe}}^{\mathrm{max}}$ to the value observed in flight.

3.4. *Deuteron Component in the Spectrometer*

The number of deuterons (N_d) among the selected positive singly charged particles was determined on the basis of the selection efficiencies for the condition $N_{\mathrm{eff}} = 0$ evaluated by means of a simulation. A large number of both deuterons and protons were generated according to the observed singly charged particle spectrum. For each event the RICH response was simulated according to P_{off} and the deflection smeared according to the high-energy SRF. Threshold fluctuations due to the refractive index variation during the flight were taken into account by generating, event by event, the value of n according to the experimental distribution. The resulting efficiencies for protons (ϵ_p) and deuterons (ϵ_d) are shown in Figure 6 as a function of the measured rigidity. In the same picture the rejection factor r, defined as $r = \epsilon_p/\epsilon_d$, is also shown. The maximum identification capability of the instrument is reached when r is minimum, that is, close to the deuteron threshold. The rigidity range for the deuteron selection was set by the requirement of a proton background level less than 50% of N_{off}, which happens between 28 and 45 GV. Data in this range were grouped into two bins to reduce statistical error on the final result. Results are summarized in Table 2. In Figure 3 the simulated distribution of background protons is compared with the observed distribution of events without Cerenkov signal in a wider rigidity range, between 10 and 100 GV. The simulation output was normalized to the total number of $Z = 1$ events in the considered rigidity range and a constant deuteron-to-proton ratio was assumed, equal to the value measured in the range 18–45 GV.

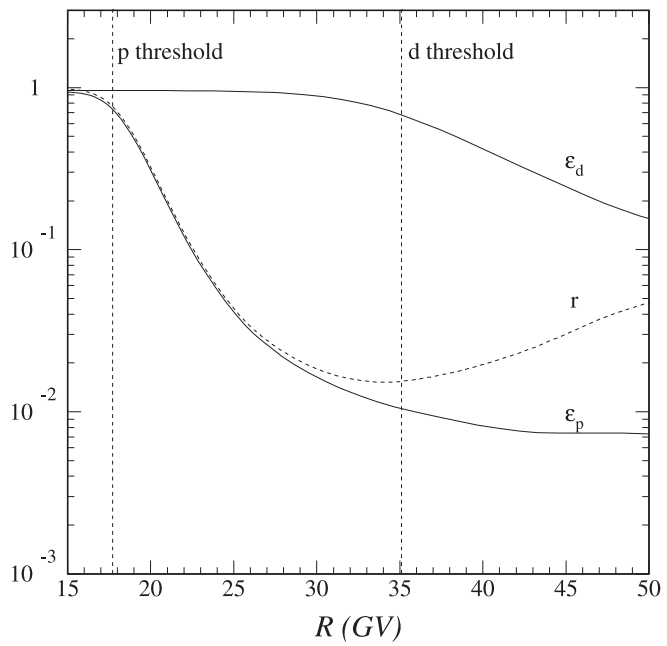

FIG. 6.—Results of the simulation. *Solid curves*: Deuteron (ϵ_d) and proton (ϵ_p) selection efficiencies for the requirement $N_{\mathrm{eff}} = 0$. *Dashed curve*: Rejection factor $r = \epsilon_p/\epsilon_d$.

The quantity N_d represents the number of deuterons detected in the apparatus. In order to obtain the number of deuterons entering the spectrometer (N_d^{sp}), the data were corrected for the finite efficiencies of the detectors and the selection cuts summarized in Table 1. These cuts were applied to select singly charged particles with a well-reconstructed track in the apparatus. The general approach followed for the CAPRICE98 experiment has been to estimate when possible the selection efficiency of each detector by using directly experimental data. This was possible thanks to the redundancy of information provided by the apparatus. The procedures used in this work, modified only to take into account the different selection parameters, were similar to the ones used to evaluate the efficiencies in previous analyses (Boezio et al. 2001, 2003a, 2003b). It was found that the efficiencies did not vary significantly over the rigidity range where deuterium selection was carried out; as a consequence, an average constant value was used. The estimated efficiencies for the conditions listed in Table 1, except for those purely geometrical, are presented in Table 3. The resulting number of deuterons in the spectrometer is presented in the first column of Table 4.

3.5. *Other Sources of Contamination*

3.5.1. *Muon Contamination*

The selected sample of positive singly charged particles contains relativistic positive muons, in addition to protons and deuterons. The order of magnitude of the muon-to-proton ratio at 20 GeV of kinetic energy and at balloon altitude is about 10^{-2} (Boezio et al. 2003a, 2003b). At this energy

TABLE 3
SUMMARY OF EFFICIENCIES FOR THE SELECTION OF SINGLY CHARGED PARTICLES (SELECTION CUTS OF TABLE 1)

DESCRIPTION	ESTIMATED VALUE (%)
Detection efficiencies:	
Tracking system	77.4 ± 0.9
Time-of-flight system	91.2 ± 0.4
RICH detector	88.5 ± 0.8
Total ($\epsilon_{Z=1}$)	62.5 ± 0.9

TABLE 4
SUMMARY OF PAYLOAD AND ATMOSPHERIC CORRECTIONS

Kinetic Energy (GeV nucleon^{-1})	Observed Number of Deuterons at Spectrometer, N_d^{sp}	Extrapolated Number at Top of Payload, N_d^{ToP}	Estimated Number of Atmospheric Secondaries, N_d^{atm}	Extrapolated Number at Top of Atmosphere, N_d^{ToA}
12.47–15.06	74.2	85.2	15.5	77.5
15.06–21.63	74.6	85.6	19.3	73.8

the probability of zero detected photoelectrons is $P_{off}(R \gg R_{th}) \sim 0.6 \times 10^{-7}$. It follows that the muon contamination is negligible.

3.5.2. *Helium Contamination*

The charge selection results in a residual contamination of helium nuclei. Since ^{4}He has approximately the same Cerenkov threshold rigidity as deuterium, helium is selected with the same efficiency as deuterons. The helium-to-proton ratio at 35 GV is about ~0.17 (Boezio et al. 2003a), and the estimated contamination of helium resulting after the charge selection is less than ~0.2%. This resulted in a total of less than one helium nucleus in the whole considered rigidity range.

3.6. *Payload and Atmospheric Corrections*

3.6.1. *Payload Corrections*

In order to reach the tracking system, the particles had to go through several material layers above the spectrometer, which included the aluminum shell of the payload, the RICH detector, and the top scintillator of the ToF system. This material corresponds, on average, to a thickness of 8.0 g cm^{-2}. To determine the number of particles at the top of the payload (N_d^{ToP}), the estimated number of particles in the spectrometer was corrected for the effect of nuclear interactions in the traversed material.

It was assumed that all the particles that interacted above the tracking system were rejected by the selection criteria. The interactions inside the spectrometer, which would not be rejected by the tracking conditions, were determined to be negligible. As a consequence, N_d^{sp} was corrected only for losses due to interactions with the material above the tracking system.

Few experimental data exist in the literature on the inelastic cross section of deuterium with nuclei. As a consequence, the deuterium nuclear interaction length for all the material traversed by the particles was evaluated by using the universal parameterization of the reaction cross section given by Tripathi et al. (1996). This parameterization was estimated to reproduce experimental data with an accuracy better than 5%. Nuclear cross sections become nearly constant above ~1 GeV nucleon^{-1}. This resulted in an energy-independent correction factor $F_{sp \to ToP} = 1.148 \pm 0.007$. Results are summarized in the second column of Table 4.

3.6.2. *Atmospheric Corrections*

To determine the number of particles at the top of the atmosphere (N_d^{ToA}), the data were corrected for both attenuation and secondary particle production in the residual atmosphere above the payload. During the propagation of cosmic rays through the atmosphere, deuterons are produced from the fragmentation of both the air target nuclei and the incoming nuclei. These secondary deuterons are indistinguishable from primary ones; thus, their contribution must be subtracted from N_d^{ToP}. In order to evaluate the number of secondary deuterons entering the apparatus, we used the code of Vannuccini et al. (2003a). In this code, a set of coupled transport equations is solved, which includes distinct equations for p, n, d, t, ^{4}He, ^{3}He, and heavy nuclei (HN), the latter being described in terms of an equivalent number of ^{12}C nuclei. For each nuclear component, the production from the spallation of heavier nuclei is considered. Production terms from the fragmentation of air target nuclei are included only in the case of nucleons and deuterons. Above a few GeV nucleon^{-1} the deuterium production is dominated by the spallation of helium and heavy nuclei.

The calculated number of secondary deuterons (N_d^{atm}) at 5.5 g cm^{-2} is summarized in the third column of Table 4. The atmospheric contribution is on average 18% of the total number of deuterons in the spectrometer. Among these, about 38% comes from heavy nuclei. The estimated uncertainty on the number of atmospheric deuterons, derived from the uncertainty on the input parameters, is about 21%.

After having subtracted the secondary component, primary data were corrected for the attenuation resulting from nuclear interactions with the residual atmosphere. The deuterium nuclear interaction length in air was estimated as described in § 3.6.1, resulting in a correction factor $F_{ToP \to ToA} = 1.113 \pm 0.006$. The obtained number of deuterons at the top of the atmosphere (N_d^{ToA}) is reported in the last column of Table 4.

3.7. *Geometrical Factor*

The geometrical factor (GF) was evaluated with Monte Carlo techniques described by Sullivan (1971). The simulation included, in addition to the geometry of the apparatus, all the selection cuts consisting in a geometrical condition (see Table 1). The value of the GF was found to be constant above ~4 GV and equal to 133.2 cm^2 sr.

3.8. *Systematic Uncertainties*

Some sources of systematic uncertainties affecting the measured abundance of deuterium at the top of the atmosphere already have been discussed. In particular, all the correction parameters related to the detector efficiencies and to the payload and atmospheric corrections have been reported in the tables and in the text with their estimated uncertainties. These uncertainties were propagated and included in the final uncertainty on N_d^{ToA}. We discuss in the following other possible sources of systematic errors:

1. *Simulation parameters*.—The evaluation of the proton background and of the deuteron selection efficiency is based on a simulation, which is affected by the uncertainty on the input parameters. The main sources of indetermination come from the uncertainties on the SRF and on P_{off}.

In § 3.3.1 two independent estimates of the SRF are described. The simulation was carried out using both the derived expressions and the results reported in § 3.4 obtained by averaging between the two. We took the difference with the

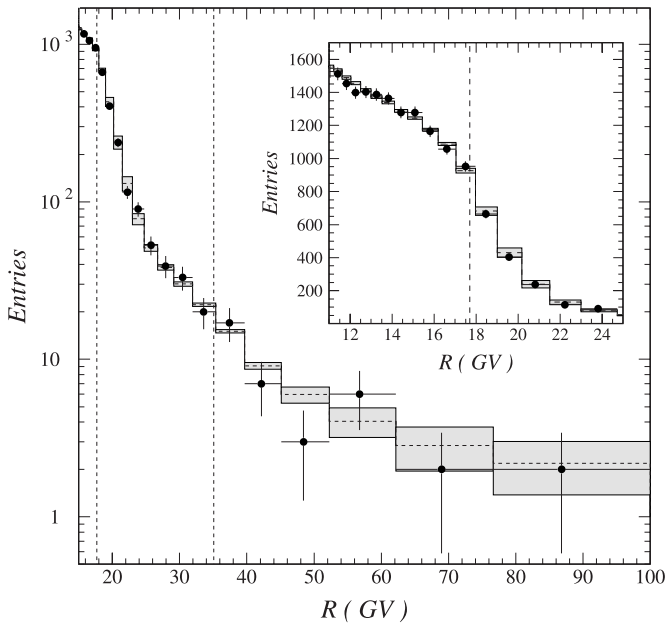

FIG. 7.—Comparison between the observed distribution of events without a Cerenkov signal and the simulated one. *Filled circles*: Experimental data. *Dashed line*: Simulated distribution; shaded rectangles show the estimated systematic uncertainty. Vertical dashed lines indicate the proton and deuteron rigidity threshold for Cerenkov light emission.

average value as an estimate of the systematic errors due to the indetermination on the SRF.

The probability $P_{\rm off}$ of zero detected photoelectrons is mainly affected by the statistical errors on the measured parameters P_0 and $N_{\rm pe}^{\rm max}$. In order to estimate the systematic effect on the simulation output, the code was run by setting the values of both parameters to $\pm 1\ \sigma$ around their best estimate. The systematic uncertainty on the number of selected deuterons N_d was evaluated as the difference with the values reported in the last column of Table 2.

The systematic uncertainties related to the simulation were assumed to be independent and the errors were quadratically summed. In Figure 7 the observed distributions of events without a Cerenkov signal between 10 and 100 GV are compared with the simulation. The total simulation uncertainty is indicated by shaded rectangles. Below the proton threshold for Cerenkov light emission the uncertainty on P_0 dominates. Above this rigidity value, both the uncertainties on the SRF and $N_{\rm pe}^{\rm max}$ contribute to the error, up to $\sim$50 GV where the indetermination on the SRF dominates. The agreement between simulation and experimental data, within the statistical and systematic errors, confirms the reliability of the simulation.

2. *Geometrical factor.*—The technique adopted to evaluate the GF was checked during the CAPRICE94 analysis (Boezio et al. 1999) using different methods. The uncertainty above 0.5 GV was found to be about 2%. A similar conclusion can be assumed for CAPRICE98.

3. *Trigger efficiency.*—The efficiency of the trigger system was measured during the preflight preparations of the instrument. It was found to be close to 100% with an uncertainty of about 2% (Boezio et al. 2001, 2003a).

4. *Atmospheric depth.*—The estimate of atmospheric secondaries and the deuterium attenuation factor are affected by the uncertainty in the residual atmosphere above the gondola. The instrument was equipped with a pressure sensor, owned and calibrated by the WiZard collaboration, which measured 5.5 ± 0.3 g cm^{-2} during the flight. An independent measurement was provided by the National Scientific Balloon Facility (NSBF), which was systematically 16% lower than that measured by our sensor. The resulting uncertainties on $N_d^{\rm atm}$ and $F_{\rm ToP\rightarrow ToA}$ partly compensate, giving an overall error on $N_D^{\rm ToA}$ of about 2%.

As a whole the systematic uncertainty on the deuterium abundance at the top of the atmosphere is dominated by the indetermination on the simulation parameters, which results in a 12%–19% error. The other sources of indetermination result in systematic uncertainties of the order of a few percent or less. All the systematic errors, except for those deriving from the different atmospheric depth measured by the NSBF, were assumed to be uncorrelated and thus were quadratically summed. The atmospheric depth given by the NSBF was instead treated as an extreme value, and the resulting uncertainties on the derived deuterium flux were summed to the other contributions.

4. RESULTS

4.1. *Deuterium Flux at the Top of the Atmosphere*

After all the corrections described in the previous sections, the deuterium flux was evaluated as follows:

$$F_d(E) = \frac{1}{\Delta E T_{\rm live} {\rm GF}} N_d^{\rm ToA}(E), \qquad (4)$$

where ΔE is the kinetic energy bin. The value of the deuterium flux is given in Table 5; in the table statistical and systematic errors are quoted separately, in order to allow a better comparison with other data. The center E of the energy bin was evaluated by calculating the center of gravity. Figure 8 shows the deuterium flux measured by CAPRICE98 compared with results from other experiments (Bogomolov et al. 2003; Webber et al. 1991; Wang et al. 2002; Aguilar et al. 2002). The data include both statistical and systematic errors. The CAPRICE98 measurement represents the first result on the deuterium flux obtained at energies above 2 GeV nucleon^{-1}. All of the other results cover an energy range that is strongly affected by solar modulation. The observed differences among

TABLE 5

DIFFERENTIAL DEUTERON FLUX AT THE TOP OF THE ATMOSPHERE VERSUS KINETIC ENERGY PER NUCLEON

Kinetic Energy Range (GeV nucleon^{-1})	Mean Kinetic Energy[a] (GeV nucleon^{-1})	$F_d \pm \delta_{\rm stat} \pm \delta_{\rm sys}$[b] [(m^2 s sr GeV nucleon^{-1})$^{-1}$]
12.47–15.06	13.66	$(6.9 \pm 1.7^{+1.0}_{-0.9}) \times 10^{-2}$
15.06–21.63	17.80	$(2.6 \pm 0.8^{+0.6}_{-0.5}) \times 10^{-2}$

[a] The mean is defined as the center of gravity.
[b] Both statistical and systematic errors are reported.

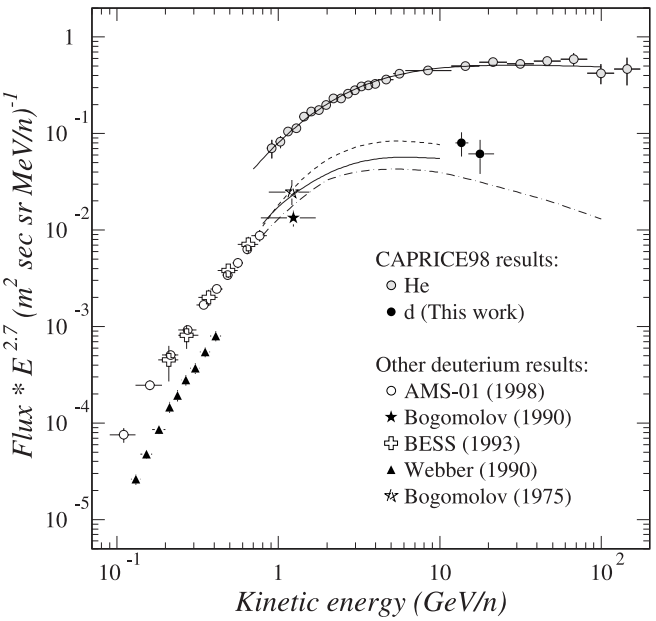

FIG. 8.—Deuterium flux. *Filled circles*: CAPRICE98 results. *Other symbols*: Other experimental results (Bogomolov et al. 2003; Webber et al. 1991; Wang et al. 2002; Aguilar et al. 2002); the year of the experiment is indicated in parentheses. Data are compared with predictions calculated from some theoretical estimations of the deuterium-to-helium ratio (see the caption of Fig. 9 for references); curves have been obtained by multiplying the helium flux measured by CAPRICE98 (*upper solid curve*) with the calculated ratio.

the measurements are indeed consistent with the corresponding solar activity (measurements performed during solar maximum are indicated by filled symbols). In the same figure the deuterium data are compared with a few theoretical predictions of the deuterium-to-helium ratio, which is discussed in the next sections. The curves in Figure 8 have been obtained by multiplying the helium flux measured by CAPRICE98 (Boezio et al. 2003a) by the calculated ratio; the upper solid curve in the picture represents a fit to the data.

4.2. *Deuterium-to-Helium Ratio*

At high energy the main production channel for deuterium is the spallation of He nuclei, even if heavier nuclei play a significant role. Thus, a meaningful quantity to study galactic propagation is the ratio d/He. The deuterium-to-helium ratio measured by CAPRICE98 is shown in Figure 9 in comparison with other experimental data and calculations.

A standard model for interpreting data on galactic cosmic rays is the modified leaky box model (MLBM). According to this model the propagation of cosmic rays is described by only one energy-dependent parameter, the escape mean free path $\lambda_{\rm esc}$, which represents the mean amount of matter traversed by cosmic rays before escaping from the confinement volume. The general approach is to tune this parameter on heavy secondary components and then use the resulting expression to evaluate the expected abundances of light secondaries. The main puzzle concerning light cosmic-ray nuclei is if their propagation history is actually the same as that of heavier nuclei.

In Figure 9 d/He experimental data are compared with different theoretical predictions based on the MLBM. It is evident that the results of the calculations, even those performed within the same propagation model, differ by a large amount. This is due to different assumptions on source spectrum and composition, fragmentation cross sections, interstellar medium (ISM)

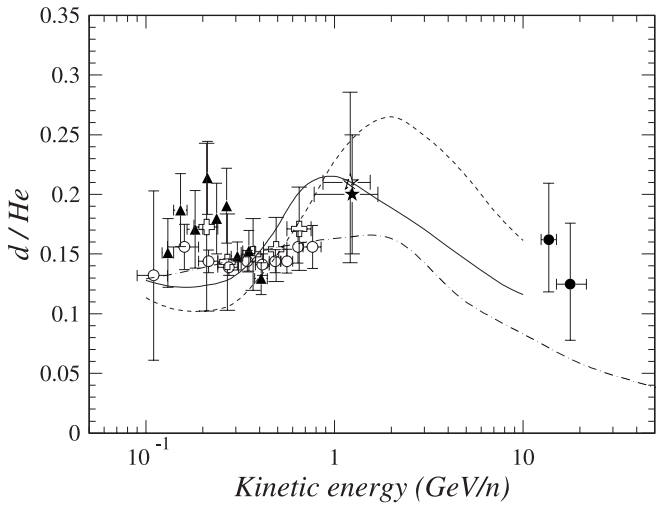

FIG. 9.—Deuterium-to-helium ratio. *Filled circles*: This work. *Other symbols*: Other experimental results (see the caption of Fig. 8 for references). Curves represent different theoretical predictions based on the MLBM. *Dashed curve*: Mewaldt (1986, 1989). *Solid curve*: Wang et al. (2002). *Dot-dashed curve*: Stephens (1989).

composition, and escape mean free path. Mewaldt (1986, 1989; Fig. 9, *dashed curve*) assumed an ISM composed of 90% H and 10% He and made use of the cross sections from Meyer (1972); these are based on low-energy experimental data, and above a few hundred MeV the proposed behavior is extrapolated on the basis of theoretical considerations. The same cross sections were used by Stephens (1989), but with an ISM composed of H only and an escape mean free path slightly lower at high energy (see Fig. 10). This resulted in a lower d/He ratio

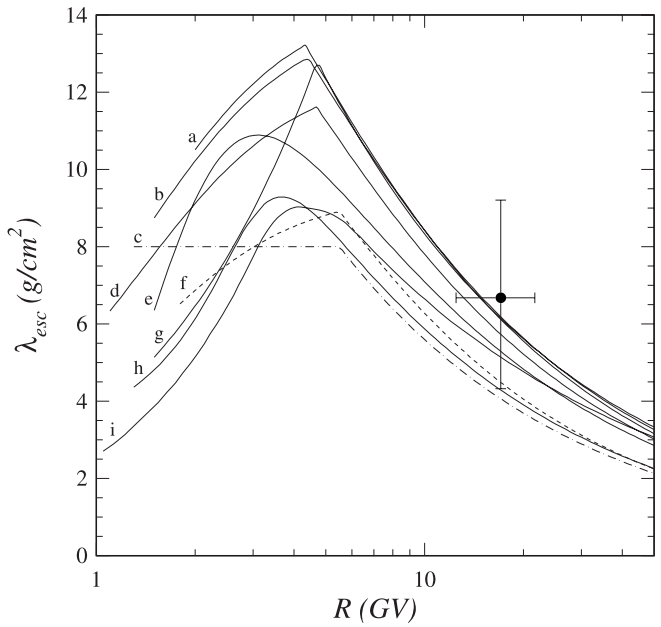

FIG. 10.—Escape mean free path of cosmic rays from the Galaxy. *Curves*: Collection of expressions derived from heavy secondary cosmic-ray data (typically B/C and sub-Fe/Fe ratios), from references (*a*) Ferrando et al. (1991), (*b*) Engelmann et al. (1990), (*c*) Stephens (1989), (*d*) Webber et al. (1996), (*e*) Yanasak et al. (2001), (*f*) Mewaldt (1986, 1989), (*g*) Molnar & Simon (2001), (*h*) García-Muñoz et al. (1987), and (*i*) Heinbach & Simon (1995). The expressions denoted with *c* and *f* are those used in the calculations shown in Fig. 9. *Experimental point*: Value inferred from the deuterium-to-helium ratio measured by CAPRICE98.

(Fig. 9, *dot-dashed curve*) at high energy. Wang et al. (2002; see also Seo et al. 1994) assumed the same escape mean free path of Stephens (1989) but made use of improved cross sections from Webber (1990), which are ~30% lower than that from Meyer (1972). Compared with Mewaldt (1986, 1989), this resulted in a lower d/He ratio at high energy (Fig. 9, *solid curve*).

At low energy the difference among the calculations is related to the solar modulation model adopted and the solar activity level assumed. The results from both Stephens (1989) and Mewaldt (1986, 1989) refer to minimum solar activity, whereas Wang et al. (2002) introduced a solar modulation level proper for the BESS 1993 flight. At high energy the solar modulation is negligible and d/He data are useful tools to constrain the propagation parameter, since the prediction is free from the uncertainty associated with solar modulation.

4.3. *Discussion of Results*

The curves shown in Figure 9 represent the few theoretical results on the d/He ratio carried out up to at least 10 GeV nucleon^{-1} that are available in the literature. In order to perform a comparison with many recent results, obtained in the framework of the MLBM, on the escape mean free path of cosmic rays heavier than helium, we estimated the same quantity for deuterium directly from the d/He ratio measured by CAPRICE98.

At high energy both solar modulation and ionization energy losses can be neglected and the transport equation for deuterium, in the MLBM approximation, reduces to an algebraic equation that can be written in the form

$$-\frac{n_d(E)}{\lambda_{\rm esc}(E)}-\frac{n_d(E)}{\lambda_d^{\rm ISM}(E)}+\sum_{k>d}\frac{n_k(E)}{\lambda_{kd}^{\rm ISM}(E)}=0, \qquad (5)$$

where n_d and n_k indicate the density of deuterium and heavier cosmic rays in the ISM, $\lambda_d^{\rm ISM}$ is the deuterium inelastic interaction length, and $\lambda_{kd}^{\rm ISM}$ is the interaction length for the inclusive production of deuterons in k+ISM reactions. From equation (5), the escape mean free path $\lambda_{\rm esc}$ can be expressed as a function of the measured d/He ratio as follows:

$$\frac{1}{\lambda_{\rm esc}}=\frac{1}{(d/{\rm He})}\left(\frac{\sum_{k>d}n_k}{n_{\rm He}}\right)\frac{1}{\langle\lambda_{kd}^{\rm ISM}\rangle_{k>d}}-\frac{1}{\lambda_d^{\rm ISM}}, \qquad (6)$$

where $\langle\lambda_{kd}^{\rm ISM}\rangle_{k>d}$ is the average interaction length for the production of deuterium in the ISM. From the available high-energy cross section measurements (Glagolev et al. 1993; Olson et al. 1983; Korejwo et al. 1999), taking into account the cosmic-ray (Simpson 1983) and ISM (90% H, 10% He) compositions, we estimated an average inclusive cross section for the production of deuterium from interactions of cosmic rays with the ISM equal to $\langle\sigma_{kd}^{\rm ISM}\rangle_{k>d}=51.4\pm4.9$ mbarn. This value is consistent with the one used by Wang et al. (2002; see also Seo et al. 1994). Using equation (6) and the deuterium-to-helium ratio measured by CAPRICE98, we found an escape mean free path $\lambda_{\rm esc}=7\pm2^{+2}_{-1}\pm1$ g cm^{-2}; the reported errors follow the notation used in Table 5, with the last term being a further systematic contribution derived from the uncertainties on cross sections and cosmic-ray composition.

The resulting value of $\lambda_{\rm esc}$ is compared in Figure 10 with a collection of expressions for the escape mean free path (García-Muñoz et al. 1987; Stephens 1989; Mewaldt 1986, 1989; Engelmann et al. 1990; Ferrando et al. 1991; Heinbach & Simon 1995; Webber et al. 1996; Molnar & Simon 2001; Yanasak et al. 2001), all obtained by fitting the secondary-to-primary ratio for heavy cosmic rays, typically B/C and sub-Fe/Fe ratios. Among these, those used by the authors of the d/He calculations shown in Figure 9 are indicated by dashed and dot-dashed curves. From Figure 10, one can see that there is a large uncertainty in the value of $\lambda_{\rm esc}$ for heavy secondary components, as a result of both cross section inputs and differing implementation of the MLBM. In particular, the oldest estimates (García-Muñoz et al. 1987; Stephens 1989; Mewaldt 1986, 1989) are systematically lower than more recent ones. As a whole, the mean amount of matter traversed by deuterium before escaping from the confinement volume inferred from the CAPRICE98 measurement is consistent with that of heavier secondary components.

This work was supported by the NASA grant NADW-110, the INFN (Istituto Nazionale di Fisica Nucleare, Italy), the ASI (Agenzia Spaziale Italiana), the DARA and DFG in Germany, the Swedish National Space Board, and the Knut and Alice Wallenberg Foundation (Sweden). Ph.D. was supported by the University of Florence and by the INFN. The Swedish-French group thanks the EC SCIENCE program for support. P. H. thanks the Swedish Foundation for International Cooperation in Research and Higher Education for support. E. M. thanks the Foundation Blanceflor Boncompagni-Ludovisi née Bildt for support. We wish to thank the National Scientific Balloon Facility and the NSBF launch crew that served in Fort Sumner. We also wish to acknowledge the essential support given by the Gas Work Group (EST/SM/SF) and the Thin Films, Section (EP/TA1/TF) at CERN, the LEPSI and CRN-Strasbourg, and the technical staff on NMSU and of INFN.

APPENDIX

THE SPECTROMETER RESOLUTION FUNCTION

The total uncertainty in the measured deflection is given by two contributions, related to the spatial resolution of the tracking system and the multiple-scattering effect; the former is energy independent and can be considered the intrinsic spectrometer resolution, while the latter decreases with increasing energy and becomes negligible above a few GV. For the deuterium analysis we needed to simulate the response of the spectrometer at high energy (above ~10 GV); thus, the knowledge of the intrinsic deflection resolution function was required. The deflection uncertainty also depends on the strength of the magnetic field along the track and on the number of position measurements used in the fit. Our approach was to derive an estimate of the SRF averaged over the sensitive volume of the tracking system defined by the cuts listed in Table 1.

Two different approaches have been proposed by Golden et al. (1991) to evaluate the resolution function for a spectrometer similar to that of CAPRICE98:

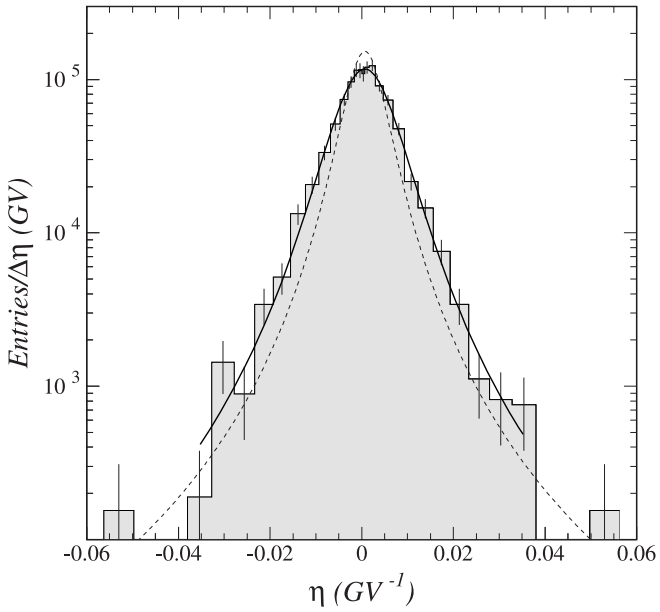

FIG. 11.—Differential distribution of relativistic muons, collected at ground level with the magnet off, as a function of the measured deflection. *Solid curve*: Fit to data. *Dashed curve*: Intrinsic SRF estimated by unfolding from the experimental distribution the multiple-scattering contribution.

1. A possible method consists in constructing the SRF on an event-by-event basis by assuming a Gaussian deflection uncertainty, with standard deviation given by the deflection error σ_η returned by the fitting routine.
2. A different empirical approach is to measure straight tracks collected with the magnet off and to take directly the resulting deflection distribution as an estimate of the SRF.

Method 1 relies on the assumption that the spatial resolution of the drift chambers is Gaussian, which is true only in first approximation. Moreover, σ_η depends on the assigned measured errors; as a consequence, it is a good estimator of the deflection uncertainty as far as the spatial resolution did not change in flight.

Method 2 was the one used in previous CAPRICE98 works (Boezio et al. 2001, 2003a), using a magnet-off data set obtained at ground prior to the flight. By means of the RICH information, particles with rigidity greater than $\sim$5 GV could be selected, for which the multiple-scattering effect is strongly reduced.

Method 1 turned out to be inadequate in this context owing to the Gaussian approximation. Method 2 allows us to overcome the restriction to a Gaussian response, but it was anyway inadequate for the CAPRICE98 deuterium analysis as a result of the residual multiple-scattering effect. Since the proton background in the deuteron sample is strongly related to the spectrometer uncertainty, a more accurate estimate of the SRF was required. As a consequence, the improved magnet-off and RICH methods described in § 3.3.1 were developed. In this appendix both methods are described in detail.

A1. MAGNET-OFF METHOD

The magnet-off method represents an improved version of method 2. An estimate of the intrinsic SRF is obtained by unfolding the contribution due to the multiple-scattering effect from the deflection distribution of relativistic muons obtained from magnet-off data.

Relativistic particles were selected by applying the same geometrical conditions listed in Table 1, plus the requirement of a measured Cerenkov angle consistent with the maximum value within 2 σ. A high value of $N_{\rm eff}$ was also required, in order to eliminate low-energy particles having a signal in the RICH detector induced by noise. Finally, low-energy electrons were eliminated with the calorimeter. The deflection distribution for the selected events (1741) is shown in Figure 11.

The unfolding procedure was based on the assumption that the intrinsic deflection uncertainty and the error due to multiple scattering are not correlated. In this approximation, the experimental deflection distribution can be considered as the convolution between the intrinsic SRF and the multiple-scattering resolution function, i.e., the distribution of deflection errors due to multiple scattering only. The latter distribution was constructed by means of a simulation code based on the GEANT-3.21 package, developed for previous balloon flights (Bocciolini et al. 1993; Boezio 1998). For the present analysis all the detectors were simulated only from the point of view of the geometry and the materials. As a consequence, the only physical process included in the simulation output related to the spectrometer was the multiple scattering with the nuclei of the various media. A large sample of muons was generated in accordance with the measured ground spectrum, with the magnetic field set to zero. For each generated event, the simulated coordinates on the tracking planes were extracted and the track was processed with the same track-fitting algorithm used on experimental data. The reconstructed Cerenkov angle was simulated on the basis of its expected value and of the measured angular resolution. Muons satisfying the requirement on $N_{\rm eff}$ were tagged by using the selection probability measured for magnet-on ground muons. The Cerenkov angle selection was applied and the deflection distribution constructed.

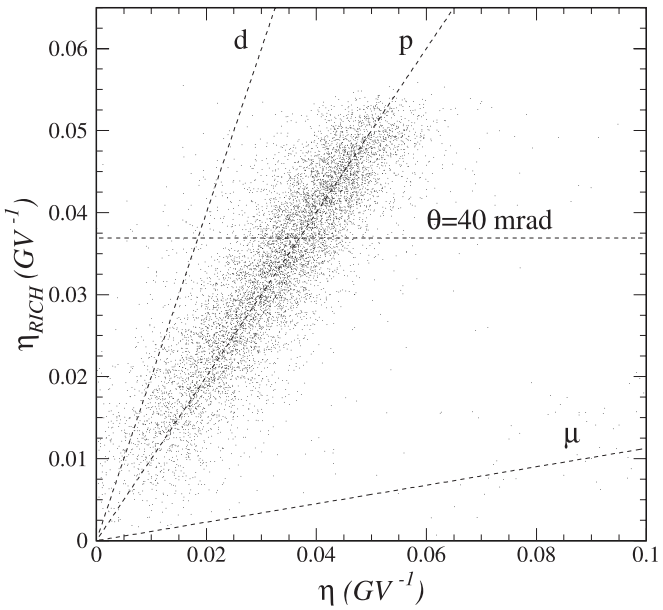

FIG. 12.—Deflection value derived from the reconstructed Cerenkov angle assuming a mass of a proton ($\eta_{\rm RICH}$) as a function of the deflection measured with the spectrometer (η), for the $Z = 1$ flight particles. *Dashed lines*: Expected values for deuterons, protons, and muons. *Horizontal dashed line*: Cut on the measured Cerenkov angle; events above this line were selected.

The experimental deflection distribution was fitted with a function obtained by convolving the simulated deflection distribution, representing the multiple-scattering resolution function, with a generalized Lorentzian function:

$$f(\delta) = \left\{1 + \left[\frac{2(\delta - p_1)}{p_2}\right]^2\right\}^{-p_3}, \tag{A1}$$

where the parameters p_1, p_2, and p_3 were obtained from the fit. The output of the fitting procedure is shown by the solid curve in Figure 11; the χ^2 was about 0.7, corresponding to ~90% CL. The dashed curve represents the resulting estimate of the SRF.

A2. RICH METHOD

The RICH method made use of the independent deflection information provided by the RICH detector. Particles were selected by applying all the basic selection cuts, listed in Table 1, plus the requirement of $N_{\rm eff} > 10$, in order to eliminate those events having a signal in the MWPC due to noise. We calculated the deflection $\eta_{\rm RICH}$ from the reconstructed Cerenkov angle assuming a mass of a proton. In Figure 12 this quantity is plotted as a function of the deflection η measured by the spectrometer. In the same plot the expected curves for particles of different types are shown.

The SRF was derived from the distribution of the variable $\xi = \eta - \eta_{\rm RICH}$. This distribution represents the SRF folded with the deflection resolution function of the RICH detector. The RICH deflection uncertainty is related to the angular resolution of the detector, described in § 2.1; the corresponding uncertainty in deflection was about $\delta\eta_{\rm RICH} \sim 0.033/R_{\rm th}({\rm GV})$ at $R = 1.1R_{\rm th}$ and increased slowly with increasing rigidity. In order to get a reliable result from the unfolding procedure, we selected only events with measured Cerenkov angle lower than 40 mrad. This cut had the advantage of both minimizing the RICH deflection uncertainty and reducing in the sample the contamination of particles other than protons (see Fig. 12). Figure 13 shows the distribution of the variable ξ obtained from the resulting sample of particles (3423 events).

The RICH deflection resolution function for the selected sample was constructed on an event-by-event basis. A large sample of protons was generated according to the observed singly charged particle spectrum, and the RICH response was simulated on the basis of the measured performances, as previously described. The selection conditions were applied and the distribution of the difference between the generated and the measured deflection was constructed.

Finally, the experimental distribution of the variable ξ, shown in Figure 13, was fitted with a function obtained by convolving the simulated RICH deflection resolution function with a generalized Lorentzian function, where parameters were left free to vary. In order to avoid having the deuteron component alter the result, the left tail of the distribution was excluded from the fit. The output of the fitting procedure is shown by the solid curve in Figure 13; the χ^2 was about 1.1, corresponding to ~30% CL. Since protons radiated above ~18 GV, multiple scattering is negligible and the SRF estimated with this method represents the intrinsic response.

A3. COMPARISON OF RESULTS

In Figure 14 the SRFs obtained by applying the four described methods are compared. The dotted curve represents the estimate obtained in the Gaussian approximation (method 1). The function was normalized to the total number of relativistic muons selected from magnet-off ground data, which are shown by experimental points in the picture. According to method 2, this distribution

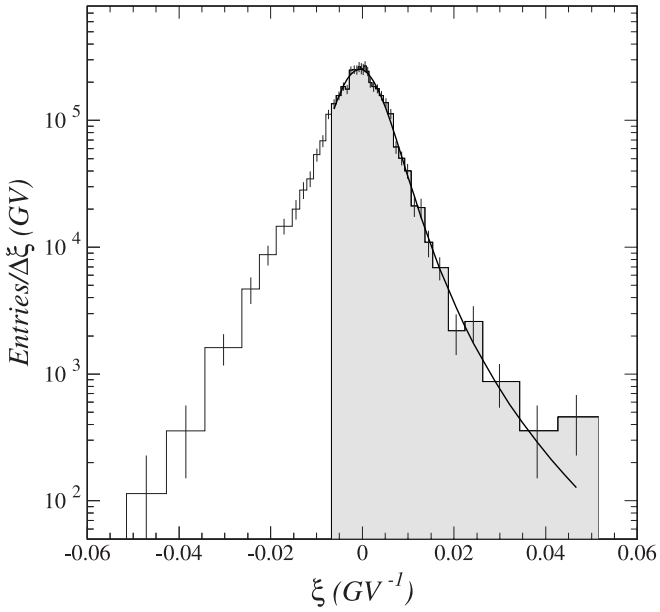

FIG. 13.—Differential distribution of $Z = 1$ flight particles as a function of the variable $\xi = \eta - \eta_{\mathrm{RICH}}$. The solid curve is a fit to data, performed in the range highlighted by the shaded area.

represents an empirical estimate of the SRF. The thin solid curve is a fit to data, performed to allow a better comparison. The thick solid curve shows the function obtained by correcting the experimental distribution for the multiple-scattering effect (magnet-off method). Finally, the thick dashed curve represents the estimate of the intrinsic spectrometer resolution function obtained with the RICH method.

As expected, the resolution function estimated with method 2 is wider than the others as a result of the effect of multiple scattering, which worsens the spectrometer resolution at low energy. Method 1 underestimates the tails of the resolution function, as a result of the Gaussian approximation. The magnet-off method and the RICH method gave results that lay approximately between the two curves, confirming the reliability of both methods. The difference between the two results is, however, significant. The results of the fit indicate a higher confidence level for the SRF estimated with the magnet-off method. However, this method is based on the assumption of two independent contributions to the deflection uncertainty, which is not exactly true as a result of the inhomogeneous magnetic field. On the other hand, the RICH method has the advantage of being representative of the spectrometer response in flight. Since both methods provided a reliable estimate of the high-energy SRF, we carried on the simulation using both evaluated functions and we derived from the difference between the two a contribution to the systematic uncertainties on the final result.

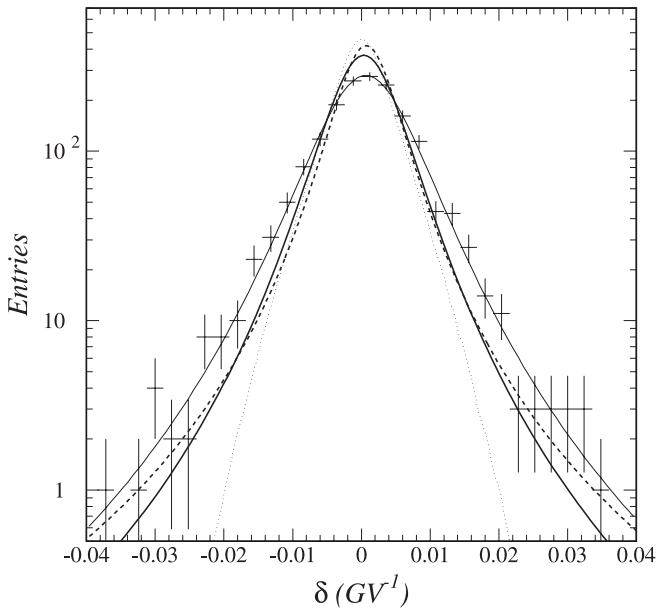

FIG. 14.—Comparison among different estimates of the SRF. *Dotted curve*: Superposition of Gaussian functions of widths distributed according to the deflection uncertainty calculated event by event by the fitting routine (method 1). *Thin solid curve and experimental points*: Distribution of the measured deflection obtained with muons from a magnet-off ground run (method 2); the curve is a fit to data performed with a generalized Lorentzian function. *Thick solid curve*: SRF obtained from magnet-off data after unfolding the contribution to the deflection uncertainty due to multiple scattering (magnet-off method). *Thick dashed curve*: SRF estimated from flight data by using the Cerenkov angle measured by the RICH detector (RICH method).

REFERENCES

Agakichiev, G., et al. 1996, Nucl. Instrum. Methods Phys. Res. A, 371, 243
Aguilar, M., et al. 2002, Phys. Rep., 366, 331
Ambriola, M., et al. 1999, Nucl. Phys. B, 78, 32
Bergström, D. 2000, Licentiat thesis, Royal Institute of Technology, Stockholm, Sweden, http://www.particle.kth.se/group_docs/astro/research/references.html
Bergström, D., et al. 2001, Nucl. Instrum. Methods Phys. Res. A, 463, 161
Bocciolini, M., et al. 1993, Nucl. Instrum. Methods Phys. Res. A, 333, 560
———. 1996, Nucl. Instrum. Methods Phys. Res. A, 370, 403
Boezio, M., 1998, Ph.D. thesis, Royal Institute of Technology, Stockholm, Sweden, http://www.particle.kth.se/group_docs/astro/research/references.html
Boezio, M., et al. 1997, ApJ, 487, 415
———. 1999, ApJ, 518, 457
———. 2001, ApJ, 561, 787
———. 2003a, Astropart. Phys., 19, 583
———. 2003b, Phys. Rev. D, 67, 072003
Bogomolov, E. A., et al. 2003, in Izvestiya RAN Phys. Series (Proceedings of Russian Academy of Sciences), 67-N4, 447
Engelmann, J. J., Ferrando, P., Soutoul, A., Goret, P., & Juliusson, E. 1990, A&A, 233, 96
Ferrando, P., Lal, N., McDonald, F. B., & Webber, W. R. 1991, A&A, 247, 163
García-Muñoz, M., Simpson, J. A., Guzik, T. G., Wefel, J. P., & Margolis, S. H. 1987, ApJS, 64, 269
Glagolev, V. V., et al. 1993, Z. Phys. C, 60, 421
Golden, R. L., et al. 1978, Nucl. Instrum. Methods Phys. Res., 148, 179
———. 1991, Nucl. Instrum. Methods Phys. Res. A, 306, 366
Heinbach, U., & Simon, M. 1995, ApJ, 441, 209
Hof, M., et al. 1994, Nucl. Instrum. Methods Phys. Res. A, 345, 561
———. 1996, ApJ, 467, L33
Korejwo, A., et al. 1999, in Proc. 26th Int. Cosmic Ray Conf. (Salt Lake City), 267
Mewaldt, R. A. 1986, ApJ, 311, 979
Mewaldt, R. A. 1989, in AIP Conf. Proc. 183, Cosmic Abundances of Matter (New York: AIP), 124
Meyer, J., P. 1972, A&AS, 7, 417
Mitchell, J., et al. 1996, Phys. Rev. Lett., 76, 3057
Molnar, A., & Simon, M. 2001, in Proc. 27th Int. Cosmic Ray Conf. (Hamburg), 1860
Olson, D. L., Berman, B. L., Greiner, D. E., Heckman, H. H., Lindstrom, P. J., & Crawford, H. J. 1983, Phys. Rev. C, 28, 1602
Ricci, M., et al. 1999, in Proc. 26th Int. Cosmic Ray Conf. (Salt Lake City), 49
Seo, E. S., McDonald, F. B., Lal, N., & Webber, W. R. 1994, ApJ, 432, 656
Shea, M. A. E., Smart, D. F., & Gentile, C. L. 1983, in Proc. 18th Int. Cosmic Ray Conf. (Bangalore), 411
Simpson, J. A. 1983, Rev. Nucl. Part. Sci., 33, 323
Stephens, S. A. 1989, Adv. Space Res., 9, 145
Sullivan, J. D. 1971, Nucl. Instrum. Methods Phys. Res., 95, 5
Tripathi, R. K., Cucinotta, F. A., & Wilson, W. W. 1996, Nucl. Instrum. Methods Phys. Res. B, 117, 347
Vannuccini, E. 2001, Ph.D. thesis, Univ. degli Studi di Firenze, http://hep.fi.infn.it/PAMELA/tesi/tesi.html
Vannuccini, E., Grimani, C., Papini, P., & Stephens, S. A. 2003a, in Proc. 28th Int. Cosmic Ray Conf. (Tsukuba), 4287
Vannuccini, E., et al. 2002, Nucl. Phys. B, 113, 88
———. 2003b, in Proc. 28th Int. Cosmic Ray Conf. (Tsukuba), 1801
Wang, J. Z., et al. 2002, ApJ, 564, 244
Webber, W. R. 1990, in AIP Conf. Proc. 203, Particle Astrophysics (New York: AIP), 294
Webber, W. R., Golden, R. L., Stochaj, S. J., Ormes, J. F., & Strittmatter, R. E. 1991, ApJ, 380, 230
Webber, W. R., Lukasiak, A., McDonald, F. B., & Ferrando, P. 1996, ApJ, 457, 435
Yanasak, N., E., et al. 2001, ApJ, 563, 768